

Gravitational waves from bubble collisions and fluid motion in strongly supercooled phase transitions

Marek Lewicki^{1,*} and Ville Vaskonen^{2,†}

¹*Faculty of Physics, University of Warsaw ul. Pasteura 5, 02-093 Warsaw, Poland*

²*Institut de Fisica d'Altes Energies, Campus UAB, 08193 Bellaterra (Barcelona), Spain*

We estimate the gravitational wave spectra generated in strongly supercooled phase transitions by bubble collisions and fluid motion. We derive analytically in the thin-wall approximation the efficiency factor that determines the share of the energy released in the transition between the scalar field and the fluid. We perform numerical simulations including the efficiency factor as a function of bubble radius separately for all points on the bubble surfaces to take into account their different collision times. We find that the efficiency factor does not significantly change the gravitational wave spectra and show that the result can be approximated by multiplying the spectrum obtained without the efficiency factor by its value at the radius $R_{\text{eff}} \simeq 5/\beta$, where β is the approximate inverse duration of the transition. We also provide updated fits for the gravitational wave spectra produced in strongly supercooled transitions from both bubble collisions and fluid motion depending on the behaviour of the sources after the collision.

I. INTRODUCTION

The first observations of gravitational waves (GWs) by LIGO/Virgo signified the beginning of a new era in astrophysics and cosmology. While up to now all observed events were produced by compact object binaries [1–4], this new messenger brings hope also for detection of primordial signals in the form of stochastic GW backgrounds. Given the tremendous advancements in sensitivity that are expected throughout a broad frequency spectrum with the upcoming experiments [5–15], the prospects for probing the early Universe processes are great even though the compact object binaries that will contribute to the stochastic GW background make the detection of its primordial components more difficult [16]. Interestingly, the recent pulsar timing observations [17–20] feature a common spectrum-process which could be an early indication of the upcoming first detection of a stochastic GW background, potentially of primordial origin [21–33].

Many high-energy processes, including phase transitions [34, 35], cosmic strings [36] and inflation [37], occurring in the early Universe may generate a detectable stochastic GW background. In this paper we focus on cosmological first-order phase transitions featured in various particle physics models. They are intensive processes where bubbles of the new phase nucleate, expand and eventually convert the whole Universe in the true vacuum phase [38]. Interactions between the expanding bubble walls and the surrounding fluid cause motion and inhomogeneities in the fluid, and both the collisions of the bubble walls and the motion of fluid inhomogeneities source GWs [39, 40]. The resulting GW spectra from these components have been extensively studied with numerical and semi-analytical methods (see e.g. [41–45] for

recent progress). These studies indicate that different sources active during the transition can produce different GW spectra.

In order to determine the GW spectrum generated in a phase transition in a given particle physics model, we need to estimate how much each of the GW sources contributes to the final GW spectrum. The vacuum energy released in the transition is split between the gradient energy of the scalar field bubble wall and motion in the fluid. How the total released energy is split depends on the strength of the interactions between the wall and the particles in the fluid, and on the strength of the transition.

In strongly supercooled phase transitions it is possible that the interactions of the bubble wall with fluid do not stop the wall from accelerating before it collides with other bubbles. In this case most of the released energy is in the bubble walls and the bubble collisions give the dominant contribution to the GW spectrum. This can happen in particular in quasi-conformal models [46–57]. If the interactions instead are sufficiently strong, the bubble wall reaches a terminal velocity before the collisions and majority of the released energy goes into fluid motion. This is the typical case in extensions of the Standard Model featuring polynomial scalar potentials [58–68].

In this paper we derive analytically an efficiency factor that determines how large is the contribution from each of the GW sources. We perform numerical simulations of the phase transition, describing both of the GW sources, bubble walls and fluid motion, in the thin-wall limit, to show how the efficiency factor affects the final GW spectrum. Moreover, we derive analytically the probability density function for the radius at which a given point on the surface of a bubble collides with another bubble and verify the results against our numerical simulations. Finally we also provide updated fits to the spectral shapes of the GW signals that can be produced by all sources active in very strong phase transitions.

* marek.lewicki@fuw.edu.pl

† vvaskonen@ifae.es

II. ENERGY BUDGET

We estimate how the energy released in the bubble expansion is shared between the scalar field gradients and the fluid motion in strongly supercooled phase transitions by studying the bubble expansion under the influence of pressure terms caused by the interactions of the wall with the ambient fluid. We perform the computation consistently in the thin-wall limit, which gives a good description of the system if the bubble reaches ultra-relativistic velocities. The following analysis improves earlier approximations used in the literature [56, 67, 69].

In the thin-wall limit the energy carried by the bubble walls can be modeled using a simple analytical prescription. This assumes that the bubble walls are spherical shells with a certain surface energy density and the interactions of the walls with the ambient fluid are local. In this limit, neglecting the expansion of the Universe, the bubble can be described by the Lagrangian [67, 70, 71]

$$L = \frac{4\pi}{3} R^3 \Delta P(R) - 4\pi\sigma R^2 \sqrt{1 - \dot{R}^2}, \quad (1)$$

where R denotes the bubble radius, dot derivative with respect to time, $\Delta P(R)$ the pressure difference across the bubble wall, and σ the surface tension of the wall. The latter is defined through the scalar potential V as [38]

$$\sigma \equiv \int_0^{\varphi_c} d\varphi \sqrt{2V(\varphi)}, \quad (2)$$

where $\varphi_c > 0$ denotes the field value at which the potential energy is the same as in the false vacuum that lies at the origin, $V(\varphi_c) = V(0)$.

In terms of the Lorentz factor of the bubble wall, $\gamma = 1/\sqrt{1 - \dot{R}^2}$, the equation of motion arising from the Lagrangian (1) is given by

$$\frac{d\gamma}{dR} + \frac{2\gamma}{R} = \frac{1}{\sigma} \left[\Delta P + \frac{1}{3} \frac{d\Delta P}{dR} \right]. \quad (3)$$

The bubble nucleates at rest, $\gamma = 1$, with an initial radius R_0 . By Eq. (3) we can relate the wall tension to the initial radius as $R_0 = 2\sigma/\Delta P_0$, where $\Delta P_0 \equiv \Delta P(R_0)$. The solution of the equation of motion can then be written as

$$\gamma = \frac{2R\Delta P(R)}{3R_0\Delta P_0} + \frac{R_0^2}{3R^2}. \quad (4)$$

The total pressure difference across the bubble wall, accounting for $1 \rightarrow 1$ scatterings and $1 \rightarrow N$ splittings at the bubble wall, is given by

$$\Delta P(R) = \Delta V - \Delta P_{1 \rightarrow 1} - \Delta P_{1 \rightarrow N}(R), \quad (5)$$

where ΔV denotes the potential energy difference between the minima. The pressure arising from $1 \rightarrow 1$ scatterings quickly reaches a constant value in the relativistic limit [71, 72]. Subsequently, the R dependence

of the total pressure difference arises only from the velocity dependence of $\Delta P_{1 \rightarrow N}$, for which we consider two forms. The first one, suggested in [73, 74] is linear in the Lorentz factor $\Delta P_{1 \rightarrow N} = \tilde{\Delta}P_{1 \rightarrow N}\gamma$, and the second one, suggested in [75, 76], is quadratic in the Lorentz factor, $\Delta P_{1 \rightarrow N} = \tilde{\Delta}P_{1 \rightarrow N}\gamma^2$. In both cases $\tilde{\Delta}P_{1 \rightarrow N}$ is a constant.

By plugging $\Delta P(R)$ into (4), we get γ as a function of R . When $\Delta P_{1 \rightarrow N} \ll \Delta V - \Delta P_{1 \rightarrow 1}$ the solution can be approximated by taking $\Delta P(R) \approx \Delta P_0$ in Eq. (4). Assuming in addition that $R \gg R_0$, the Lorentz factor grows linearly with the radius, $\gamma \approx 2R/(3R_0)$. Eventually, as the bubble wall accelerates, γ becomes large enough for the $1 \rightarrow N$ splittings to be important, $\Delta P_{1 \rightarrow N} \sim \Delta V - \Delta P_{1 \rightarrow 1}$, after which it asymptotically reaches the value

$$\gamma_{\text{eq}} \equiv \left[\frac{\Delta V - \Delta P_{1 \rightarrow 1}}{\tilde{\Delta}P_{1 \rightarrow N}} \right]^{\frac{1}{c}}, \quad (6)$$

where $c = 1, 2$ depending on the scaling of the $1 \rightarrow N$ pressure, $\Delta P_{1 \rightarrow N} \propto \gamma^c$. The change from the linear growth to asymptotically constant behaviour occurs when the radius reaches

$$R_{\text{eq}} \equiv \frac{3}{2} R_0 \gamma_{\text{eq}}. \quad (7)$$

The solution $\gamma(R)$, expanded to the leading order in $\gamma_{\text{eq}} \gg 1$, can be written as¹

$$\frac{\gamma(R)}{\gamma_{\text{eq}}} = \begin{cases} \left(1 + \frac{R_{\text{eq}}}{R}\right)^{-1}, & c = 1, \\ \sqrt{\left(\frac{R_{\text{eq}}}{2R}\right)^2 + 1} - \frac{R_{\text{eq}}}{2R}, & c = 2. \end{cases} \quad (8)$$

In Fig. 1 we show $\gamma(R)$ for different values of γ_{eq} for both $\Delta P_{1 \rightarrow N} \propto \gamma$ (solid) and $\Delta P_{1 \rightarrow N} \propto \gamma^2$ (dashed). In both cases the transition from linear growth, $\gamma \propto R$ to the constant value $\gamma \approx \gamma_{\text{eq}}$ is quite fast, and the difference between the two cases is small. The main effect of the scaling of $\Delta P_{1 \rightarrow N}$ is that it changes γ_{eq} and R_{eq} .

We define the efficiency factor κ as the fraction of the total released energy within a unit solid angle that goes into the bubble wall energy,

$$\kappa(R) = \frac{3(\gamma R^2 - R_0^2)\sigma}{(R^3 - R_0^3)\Delta V}. \quad (9)$$

The rest of the released energy, $1 - \kappa(R)$, goes into fluid motion. This is a good approximation for strongly supercooled transitions. In weaker transitions one also needs to keep in mind that some of the energy going into the fluid will be lost on its heating which will reduce the overall GW signal from the fluid motion [67, 77].

¹ Also the full solution is analytic, but not illustrative. For $c = 1$, the next term in the expansion of $\gamma(R)$ is $\propto \gamma_{\text{eq}}^0$, but suppressed by another power of $1 + R_{\text{eq}}/R$, and for $c = 2$, the next term is $\propto \gamma_{\text{eq}}^{-1}$.

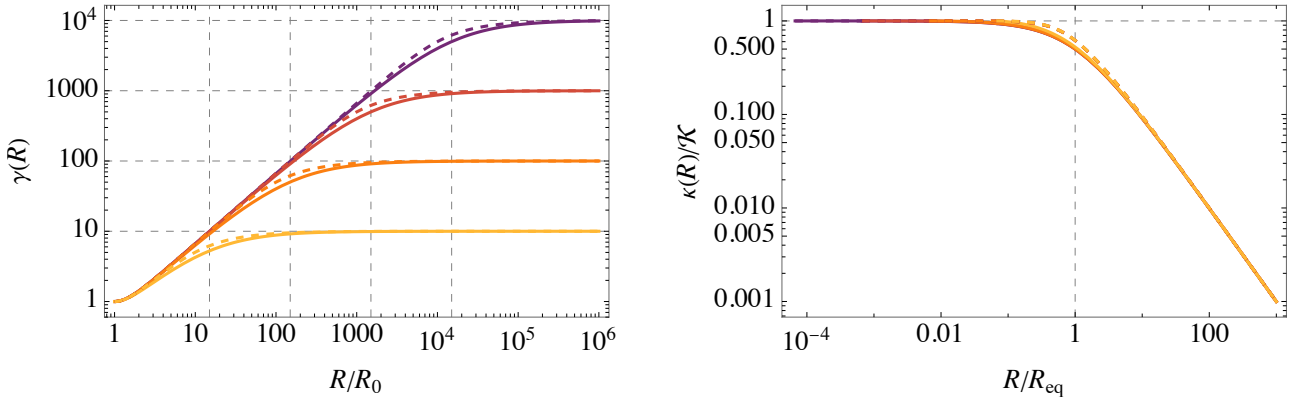


FIG. 1. The Lorentz factor of the bubble wall (left panel) and the efficiency factor κ (right panel) as a function of the bubble radius R for $\gamma_{\text{eq}} = 10, 100, 10^3, 10^4$ from light to dark. The solid black curves show the case $\Delta P_{1 \rightarrow N} \propto \gamma$ and the orange dashed curves the case $\Delta P_{1 \rightarrow N} \propto \gamma^2$. In the left panel the vertical dashed lines indicate the values of R_{eq}/R_0 .

Using the approximation (8), we can express the efficiency factor as

$$\kappa(R) \approx \mathcal{K} \frac{R_{\text{eq}}}{R} \frac{\gamma(R)}{\gamma_{\text{eq}}}, \quad (10)$$

where

$$\mathcal{K} \equiv \left[1 - \frac{\alpha_{\infty}}{\alpha} \right] \left[1 - \frac{1}{\gamma_{\text{eq}}^c} \right] \quad (11)$$

is a constant, $\mathcal{K} < 1$. The parameters α and α_{∞} are defined by scaling with the radiation energy density ρ_R as $\alpha = \Delta V/\rho_R$ and $\alpha_{\infty} = \Delta P_{1 \rightarrow 1}/\rho_R$ (see [67] for more details). Typically for strongly supercooled transitions $\mathcal{K} \approx 1$. As shown in the right panel of Fig. 1, the efficiency factor remains constant at $R \ll R_{\text{eq}}$ and decreases as $\kappa \propto 1/R$ at $R \gg R_{\text{eq}}$. In the same way as for $\gamma(R)$, the difference between the cases $\Delta P_{1 \rightarrow N} \propto \gamma$ and $\Delta P_{1 \rightarrow N} \propto \gamma^2$ is small.

III. BUBBLE NUCLEATION AND COLLISIONS

Soon after the bubble has nucleated, we can neglect its initial radius, and, if the friction terms are sufficiently small ($\gamma_{\text{eq}} \gg 1$), we can approximate that the bubble radius grows as $R = t - t_n$, where t_n denotes the nucleation time of the bubble. Moreover, assuming that the bubbles are much smaller than the Hubble horizon, we can neglect the expansion of the Universe. The expected number of bubbles reaching a given point is then given by

$$N(t) = \frac{4\pi}{3} \int_{-\infty}^t dt' (t - t')^3 \Gamma(t'), \quad (12)$$

where $\Gamma(t)$ denotes the bubble nucleation rate per unit time and volume, and the probability that the given point still is in the false vacuum at time t is

$$P(t) = e^{-N(t)}. \quad (13)$$

Let us consider a bubble nucleation rate $\Gamma(t) = C e^{A(t)}$. Around the time t_* when the transition proceeds, we can expand $A(t)$ to get $\Gamma(t) = C e^{A(t_*) + \beta(t - t_*)} = \Gamma_0 e^{\beta t}$, where $\beta \equiv d \ln \Gamma / dt|_{t=t_*}$ and $\Gamma_0 \equiv C e^{A(t_*) - \beta t_*}$. As the transition is not an instantaneous process, the choice of t_* includes some ambiguity. It is convenient to choose t_* by requiring that $P(t_*) = 1/e$, which gives $\Gamma_0 = \beta^4/(8\pi)$, and $N(t) = e^{\beta t}$.

Next, let us consider a point on the surface of a bubble that nucleated at time t_n . If the point is still in the false vacuum when the radius of the bubble is R , then it has stayed in the false vacuum for the whole time $0 \leq t - t_n < R$. The probability for this is $P(t_n + R)$. So, the probability that a bubble nucleated within time $t_n < t < t_n + dt_n$ in a volume V , and that a point on its surface is still in the false vacuum at radius R , is given by $dt_n V \Gamma(t_n) P(t_n + R)$. By integrating this over the nucleation time t_n we get the probability density function for the radius at which a bubble surface element collides with the surface of another bubble,

$$p(R_c) \propto \int dt_n \Gamma(t_n) P(t_n + R_c), \quad (14)$$

which we normalize to unity, $\int dR_c p(R_c) = 1$. For the exponential bubble nucleation rate, $\Gamma(t) \propto e^{\beta t}$, this gives (independently of the prefactor Γ_0)

$$p(R_c) = \beta e^{-\beta R_c}. \quad (15)$$

The above result provides a good cross-check for the numerical simulations that we will use for the GW computation. In Fig. 2 the solid curve and the gray band indicate the mean and variance of the R_c distribution obtained from 90 simulations with simulation volume $(16/\beta)^3$ and each of the simulation including at least 70 bubbles. In these simulations we nucleate thin-wall bubbles according to the exponential rate inside a cubic box with periodic boundary conditions, evolve them according to $R = t - t_n$, discretise the bubble surfaces, and find

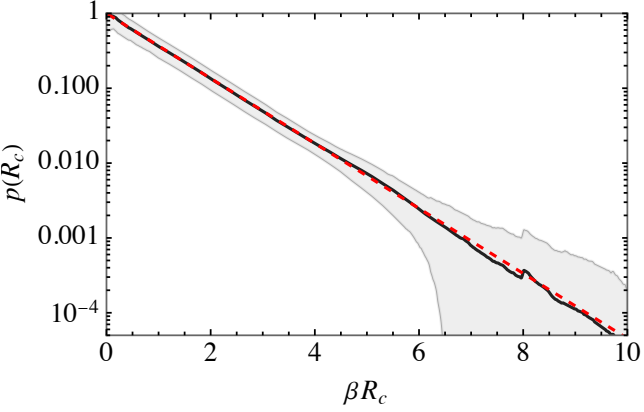


FIG. 2. Probability distribution function of bubble radius at collision. The red dashed curve shows the analytical result (15). The black curve and the gray band show the mean and the variance of the result from our numerical simulations of bubble nucleation.

the radius at which each of the points on the bubble surface collide with a wall of another bubble using the cosine rule. We label the bubbles with index j and denote the position vectors of the bubble centers by \vec{x}_j . Consider a point defined by the angles θ and ϕ on the surface of the bubble $j = j'$. The radius at which that point collides with a surface of another bubble is given by

$$R_c = \min_{j \neq j'} \left[\frac{d_j^2 - \Delta t_j^2}{2(d_j \cos \theta_j - \Delta t_j)} \right], \quad (16)$$

where the minimum is taken over all bubbles, $d_j^2 \equiv |\vec{x}_j - \vec{x}_{j'}|^2$ is the distance between the bubble nucleation centers, $\Delta t_j \equiv t_{n,j} - t_{n,j'}$ is the time between their nucleation, and θ_j is the angle between the vector $\vec{x}_j - \vec{x}_{j'}$ and the vector corresponding to the angles θ and ϕ . As shown in Fig. 2, the simulation result agrees well with the analytical result (15).

A widely used approximation for the bubble radius upon collision comes from the bubble number density $n_{\text{bubbles}} = \int dt_n \Gamma(t_n) P(t_n)$ which leads to $R_* = n_{\text{bubbles}}^{-1/3} = (8\pi)^{1/3}/\beta$. From $p(R_c)$ we can calculate moments of the bubble radius when a bubble surface element collides with the surface of another bubble, $\langle R_c^n \rangle = \int dR_c R_c^n p(R_c)$. For the exponential bubble nucleation rate this gives

$$\langle R_c^n \rangle = n! \beta^{-n}. \quad (17)$$

Given that the released energy scales with the radius to the third power, this leads to a different estimate of the average bubble radius $R_* = \langle R_c^3 \rangle^{1/3} = 6^{1/3}/\beta$ more appropriate for computation of the GW spectrum.

IV. GRAVITATIONAL WAVES

The energy released in the bubble expansion is divided between the bubble wall and the fluid shell that follows

right behind the wall. Both the bubble walls and the fluid shells source GWs. We model these sources in the thin-wall limit and calculate the GW spectrum accounting for the efficiency factor $\kappa(R)$ for the bubble collisions and $1 - \kappa(R)$ for the fluid motion. The modeling of the fluid motion in the thin-wall limit is based on the assumption that the released energy going to fluid motion is strongly localized in a thin shell. Before collision this fluid shell is right behind the bubble wall and after the collision it propagates to the same direction as before the collision, however, depending on how strong the interaction are between the fluid and the scalar field, it's velocity can slow down to the speed of sound.

We calculate the GW spectrum as e.g. in Refs. [43, 44] assuming that, as in the previous section, the bubble nucleation follows exponential rate per unit volume, $\Gamma \propto e^{\beta t}$. Each of the contributions ($l = \text{bubbles, fluid}$) to the resulting energy spectrum of GWs can be expressed as

$$\Omega_{\text{GW},l}(f) = \left[\frac{H}{\beta} \right]^2 \left[\frac{\alpha}{1 + \alpha} \right]^2 S_l(f), \quad (18)$$

where

$$S_l(f) = \left(\frac{2\pi f}{\beta} \right)^3 \frac{3\beta^5}{2V_s} \int \frac{d\Omega_k}{4\pi} [|C_{l,+}(f)|^2 + |C_{l,\times}(f)|^2] \quad (19)$$

encodes the spectral shape of the signal. The integral is over the wavevector \vec{k} directions, and the integrand is $\propto V_s/\beta^5$ if the volume V_s over which we average the GW energy spectrum is sufficiently big.

Using the thin-wall limit, the functions $C_{l,+}$ and $C_{l,\times}$ in the direction $\hat{k} = (0, 0, 1)$, can be expressed as

$$C_{l,+,\times}(f) \approx \frac{1}{6\pi} \sum_j \int_{t_{n,j}} dt d\Omega \sin^2 \theta g_{+,\times}(\phi) \times R_j^3 f_l(R_j) e^{i2\pi f(t - z_j - R_j \cos \theta)}. \quad (20)$$

The sum runs over all the bubbles nucleated in the volume V_s , $t_{n,j}$ is the time of nucleation of the bubble j , z_j is the z coordinate of its center, and $R_j = v_l(t - t_{n,j})$, where v_l is the bubble wall/fluid shell velocity, denotes the radius of the bubble/fluid shell j at time t . For the bubble walls we use $v_{\text{bubbles}} = 1$ both before and after the collision, whereas for the fluid shells we use $v_{\text{fluid}} = 1$ before the collision and after the collision we consider two cases: $v_{\text{fluid}} = 1$ and $v_{\text{fluid}} = c_s = 1/\sqrt{3}$. The former is appropriate for very strong transitions [78], whereas the latter is realized for weaker transitions [45]. The functions $g_{+,\times}$ read $g_+(\phi) = \cos(2\phi)$ and $g_\times(\phi) = \sin(2\phi)$.

The function $f_l(R)$ encodes the scaling of the GW source [44]. For the bubble collisions contribution, we follow the results of lattice simulations [43, 44], which showed that the maximum of the stress-energy tensor scales as $T_{rr} \propto R^{-\xi}$ after the collision. The power ξ in general depends on the underlying particle physics model. In particular, it was shown in [43] that breaking of a global symmetry corresponds to $\xi = 2$ while in [44]

it was shown that in models where the phase transition breaks a gauge symmetry correspond to $\xi = 3$. Accounting also for the efficiency factor κ , the f_l function for bubble collisions is given by

$$f_{\text{bubbles}}(R) = \begin{cases} \kappa(R), & R \leq R_c, \\ \kappa(R_c) \left[\frac{R_c}{R} \right]^{\xi+1}, & R > R_c, \end{cases} \quad (21)$$

where R_c denotes the bubble radius at the moment of collision, $t = t_c$. In contrast with Refs. [43, 44], where R_c was determined numerically by the bisection method, we find R_c using Eq. (16).

Also for the fluid motion we assume that the maximum of the stress-energy tensor scales as $R^{-\xi}$ after the collision. The function f_l for fluid motion then reads

$$f_{\text{fluid}}(R) = \begin{cases} 1 - \kappa(R), & R \leq R_c, \\ [1 - \kappa(R_c)] \left[\frac{R_c}{R} \right]^{\xi+1}, & R > R_c. \end{cases} \quad (22)$$

In the perfect fluid description, that assumes the fluid to remain in local equilibrium at all times, the transverse-traceless part of the stress energy tensor of the fluid reads $T_{ij} = \gamma^2 v_i v_j w$, where \vec{v} is the fluid velocity and w is its enthalpy density. By the interactions of the fluid with the wall, an overdense fluid shell with radial velocity $v_r > 0$ builds up around the bubble wall. If the wall reaches a terminal velocity, the fluid shell settles into a self-similar profile [77]. The shell continues to propagate after the bubble wall collides with the wall of another bubble. We track the consequent evolution of the fluid shell with a simplified lattice simulation assuming spherical symmetry [45, 79]. As shown in Fig. 3, we find that the maximum of the rr component of the stress energy tensor reaches $T_{rr} \propto R^{-3}$ scaling soon after the collision. This motivates us to consider $\xi = 3$ for the scaling of the fluid related GW source. For comparison, we consider also $\xi = 2$ which corresponds to the bulk flow model [80].

For certain simple forms of the f_l function the time integral in Eq. (20) can be done analytically, which makes the simulation significantly faster. In particular, it can be done analytically if f_l is a broken power-law with integer powers. We consider the form (10) for the efficiency factor κ with $c = 1$. Strictly speaking our results then hold for the case that $\Delta P_{1 \rightarrow N} \propto \gamma$. However, since the difference in $\kappa(R)$ for $c = 1$ and $c = 2$ is very small, our results give a good approximation also of the case $\Delta P_{1 \rightarrow N} \propto \gamma^2$. The pressure $\Delta P_{1 \rightarrow N}$ mainly just determines the asymptotic radius R_{eq} through Eqs. (7) and (6). In our simulations R_{eq} is an input parameter, and we perform the numerical simulations for several values of R_{eq} . We also assume that $\mathcal{K} \approx 1$, which typically holds for strongly supercooled transitions, so that

$$\kappa(R) \approx \frac{1}{1 + R/R_{\text{eq}}}. \quad (23)$$

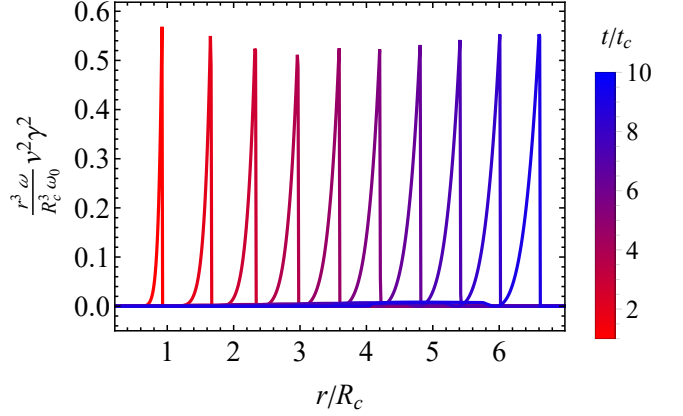


FIG. 3. Time evolution of the perfect fluid stress energy tensor scaled with the distance from the center of the bubble to third power. The red initial profile is the initial condition just after the bubble collision t_c and darker colours show the profile at later times. The parameters for this example profile are $\alpha = 0.5$ and $v_w = 0.93$ corresponding to a not too strong transition such that the velocity of the profile quickly changes to the speed of sound.

V. RESULTS

We perform 90 simulations with simulation volume $(16/\beta)^3$, each including at least 70 bubbles, for a range of R_{eq} values including both signals due to bubble walls and the surrounding fluid in each of the cases described in the previous section. From the simulations we compute the spectral shape function (19). In each case we fit the data combined from the 90 simulations with a broken power-law spectrum of the form

$$S_{\text{fit}}(f) = \frac{A (a + b)^c}{\left[b \left(\frac{f}{f_p} \right)^{-\frac{a}{c}} + a \left(\frac{f}{f_p} \right)^{\frac{b}{c}} \right]^c}, \quad (24)$$

where $a, b > 0$ determine the low and high frequency power-law tails of the spectrum, $c > 0$ the width of the transition between these power-laws, while f_p and A the peak frequency and amplitude of the spectrum respectively. The resulting GW spectra are shown in Fig. 4 with the solid curves. The color coding indicates different values of R_{eq} .

For the solid curves in Fig. 4 the efficiency factor is directly included in the simulation as in Eqs. (21) and (22). A commonly used approximation for the effect of the efficiency factor on the GW spectrum is to multiply the spectra obtained for bubble collisions and fluid motion without any efficiency factor by $\kappa(R_{\text{eff}})^2$ and by $(1 - \kappa(R_{\text{eff}}))^2$, respectively. To check this, we have computed the amplitude of the GW spectrum in each case relative to the R_{eq} case that gives the largest amplitude and fitted R_{eff} . The data points and resulting fits for all cases are shown in Fig. 5 and the corresponding fitted values of R_{eff} in the last line of Table I. We find that

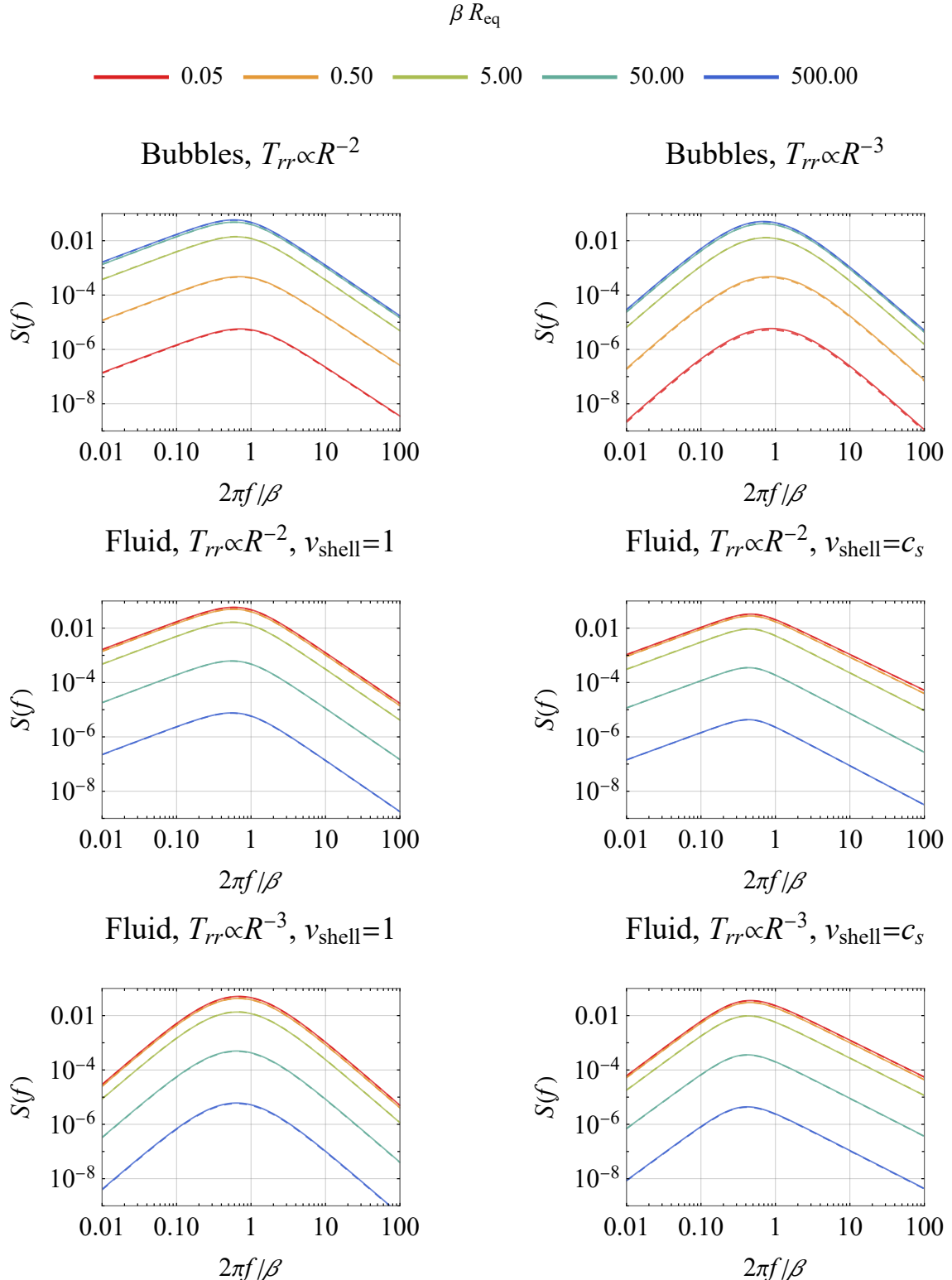


FIG. 4. Fitted GW spectral shape sourced by bubble walls and fluid motion assuming different scalings of the source after the collisions, $T_{rr} \propto R^{-\xi}$, and different velocities of the fluid shell after the collision. The solid curves show the results obtained by directly including the factor $\kappa(R)$ to the simulation and the dashed curves the result obtained by scaling the result obtained without it factor by $\kappa(R_{\text{eff}})$.

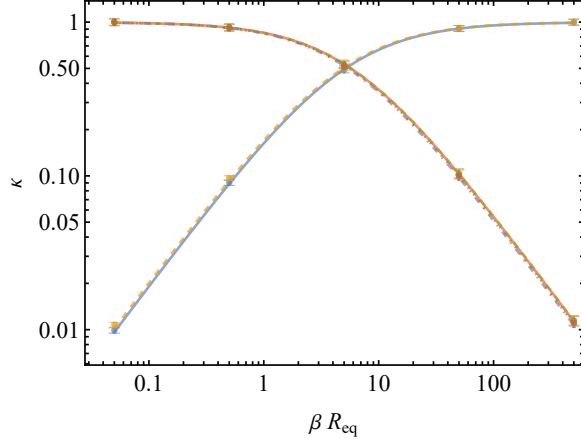


FIG. 5. The blue and red points with error bars show the amplitude of the GW spectrum from bubble collisions and from fluid motion, respectively, relative to the R_{eq} value that gives the largest amplitude. The blue and red curves show κ_{bubbles} and κ_{fluid} , respectively. The parameters read $\xi = 3$ and $v_{\text{fluid}} = 1$ for both solid lines and the points of corresponding colour. Dashed and dotted lines and their corresponding points show the remaining cases ($\xi = 2$ and $v_{\text{fluid}} = c_s$) which as we see largely overlap with the previous two.

the effect of the efficiency factor is almost independent of the behaviour of the GW source after the collisions. In all cases our results give $R_{\text{eff}} \simeq 5/\beta$, showing that the often used approximation with $R_{\text{eff}} = (8\pi)^{1/3}/\beta \approx 2.9/\beta$ slightly underestimates R_{eff} . Moreover, the results of applying the fitted efficiency factor are shown in Fig. 4 by the dashed curves. For these curves we have used the mean values given in Table I that are obtained by averaging over the fits with different equilibrium radius, except for the amplitude for which we use the strongest signal for each source. We see that the dashed curves agree very well with the fully numerical results shown by the solid curves. This shows that the efficiency factor does not change the shape of the GW spectrum but gives only an overall suppression factor.

To summarize, we have shown that for very strong transitions, $\alpha \gg \alpha_\infty$, the GW spectrum from bubble collisions and from fluid motion, accounting for the distribution of energy between these sources, is given by

$$\Omega_{\text{GW}}(f) = \left[\frac{H}{\beta} \right]^2 \left[\frac{\kappa(R_{\text{eff}}) \alpha}{1 + \alpha} \right]^2 \frac{A(a + b)^c}{\left[b \left(\frac{f}{f_p} \right)^{-\frac{a}{c}} + a \left(\frac{f}{f_p} \right)^{\frac{b}{c}} \right]^c}, \quad (25)$$

where the efficiency factor is given by Eq. (23). The fitted values of the parameters A, a, b, c, f_p and R_{eff} are given in Table I. For weaker transitions, $\alpha \lesssim \alpha_\infty$, also the prefactor \mathcal{K} , given in Eq. (11), needs to be accounted for, as well as the suppression arising from heating of the fluid around the bubble wall [77]. In the limit of large wall velocity appropriate for strong transitions this

reduction takes a simple form [67]

$$\kappa_{\text{fluid}} = \frac{\alpha_{\text{eff}}}{\alpha} \frac{\alpha_{\text{eff}}}{0.73 + 0.083\sqrt{\alpha_{\text{eff}}} + \alpha_{\text{eff}}}, \quad (26)$$

where $\alpha_{\text{eff}} = [1 - \kappa(R_{\text{eff}})]\alpha$.

The GW spectrum today can be obtained from (25) by accounting for the scaling of the amplitude and frequency with the scale factor [43]:²

$$\Omega_{\text{GW},0} = \frac{1.67 \times 10^{-5}}{h^2} \left[\frac{100}{g_*} \right]^{\frac{1}{3}} \Omega_{\text{GW}}(f), \quad (27)$$

$$f_{p,0} = h_* \left[\frac{f_p}{\beta} \right] \left[\frac{\beta}{H} \right],$$

where h denotes the dimensionless Hubble constant, $h = 0.674$ [82], and h_* the inverse Hubble time at the transition redshifted to its value today

$$h_* = 1.65 \times 10^{-5} \text{ Hz} \left[\frac{T_*}{100 \text{ GeV}} \right] \left[\frac{g_*}{100} \right]^{\frac{1}{6}}. \quad (28)$$

Here T_* denotes the temperature after the transition (including reheating) and g_* the effective number of relativistic degrees of freedom at that temperature. At scales larger than the horizon scale at the time of the transition the source is not coherent and, consequently, in standard radiation domination the slope of the spectrum changes to $\Omega_{\text{GW}} \propto f^3$ for $f < h_*$ [83, 84].³

VI. CONCLUSIONS

In this paper we have revisited the energy budget of strong first-order phase transitions to verify its impact on the produced gravitational wave spectra. We have gone beyond the current state-of-art by including the efficiency as a function of radius of the bubble accounting for the collision time of each point on the bubble surface. We have utilised numerical simulations randomly nucleating bubbles in a three dimensional box with periodic boundaries and used these to compute the GW spectra. This has allowed us to confirm that a simplified treatment of simply scaling entire spectra with an efficiency factor computed at some characteristic radius is accurate as the spectral shapes do not change due to the efficiency factor significantly. We did, however, find

² Here for simplicity while red-shifting we assumed radiation dominated expansion from the transition time up to the matter-radiation equality. For a review of alternative scenarios and their impact on the spectra see Ref. [81].

³ The low frequency slope is also changed by possible modifications of the expansion rate [85–87] although the only scenario in which the signal is not diminished is when the modification in question is itself caused by the transition for instance through slow decay of the scalar field leading to a period of matter domination [56].

	Bubbles			Fluid			
	envelope	$T_{rr} \propto R^{-2}$	$T_{rr} \propto R^{-3}$	$T_{rr} \propto R^{-2}$		$T_{rr} \propto R^{-3}$	
		$v_{\text{fluid}} = 1$	$v_{\text{fluid}} = c_s$	$v_{\text{fluid}} = 1$	$v_{\text{fluid}} = c_s$	$v_{\text{fluid}} = 1$	$v_{\text{fluid}} = c_s$
100 A	3.78 \pm 0.04	5.93 \pm 0.05	5.13 \pm 0.05	5.94 \pm 0.02	3.36 \pm 0.01	5.14 \pm 0.04	3.64 \pm 0.02
a	3.08 \pm 0.04	1.03 \pm 0.04	2.41 \pm 0.10	1.03 \pm 0.05	1.00 \pm 0.05	2.36 \pm 0.09	2.02 \pm 0.08
b	0.98 \pm 0.05	1.84 \pm 0.17	2.42 \pm 0.11	1.87 \pm 0.18	1.39 \pm 0.15	2.36 \pm 0.09	1.38 \pm 0.06
c	1.91 \pm 0.29	1.45 \pm 0.34	4.08 \pm 0.77	1.39 \pm 0.38	0.71 \pm 0.26	3.69 \pm 0.48	1.48 \pm 0.32
$2\pi f_p/\beta$	1.33 \pm 0.19	0.64 \pm 0.09	0.77 \pm 0.12	0.57 \pm 0.04	0.44 \pm 0.04	0.66 \pm 0.04	0.44 \pm 0.04
βR_{eff}	4.10 \pm 0.31	5.07 \pm 0.51	4.81 \pm 0.45	5.66 \pm 0.51	5.71 \pm 0.52	5.34 \pm 0.49	5.47 \pm 0.50

TABLE I. Fitted values for the parametrization of the spectral shape (24) and fitted value of βR_{eff} in Eq. (23). The corresponding spectra are shown in Fig 5.

that in order to accurately describe the results the characteristic radius used in the simplified calculation should be around $R_{\text{eff}} \approx 5/\beta$ rather than the usually employed average bubble separation $R_* = (8\pi)^{1/3}/\beta \approx 2.9/\beta$.

In each simulation we have also took into account the scaling of the GW sources after the collision in order to provide new fits for the resulting spectra from strongly supercooled transitions. The results are shown in Table I and, starting from strongest transitions, include bubble collision spectra for both $T_{rr} \propto R^{-3}$, appropriate for gauge symmetry breaking, and $T_{rr} \propto R^{-2}$, appropriate for global symmetry breaking. Going towards slightly weaker transitions, we have provided the spectrum generated by fluid motion with the scaling $T_{rr} \propto R^{-3}$ and assuming the fluid remains in the form of relativistic shocks $v_{\text{fluid}} = 1$ after the transition. For transitions which are not extremely strong, we have show results closer to the sound wave picture in which the velocity of the fluid quickly relaxes to the speed of sound $v_{\text{fluid}} = c_s$, again assuming the scaling $T_{rr} \propto R^{-3}$. Finally, for illustration, we also provide fluid spectra assuming the scaling $T_{rr} \propto R^{-2}$.

Taking into account that for very relativistic walls the fluid profiles are extremely peaked, we have thus show

that the final GW spectrum will be indistinguishable from an even stronger transition where bubble collisions would be the main source. Only for weaker transitions where the hydrodynamical effects change the propagation speed of the fluid shells, the spectrum diverges from the spectrum arising from bubble collisions.

ACKNOWLEDGMENTS

Acknowledgments – This work was supported by the Spanish MINECO grants IJC2019-041533-I, FPA2017-88915-P and SEV-2016-0588, the Spanish MICINN (PID2020-115845GB-I00/AEI/10.13039/501100011033), the grant 2017-SGR-1069 from the Generalitat de Catalunya, the Polish National Science Center grant 2018/31/D/ST2/02048, and the Polish National Agency for Academic Exchange within Polish Returns Programme under agreement PPN/PPO/2020/1/00013/U/00001. IFAE is partially funded by the CERCA program of the Generalitat de Catalunya.

[1] B. P. Abbott *et al.* (LIGO Scientific, Virgo), GWTC-1: A Gravitational-Wave Transient Catalog of Compact Binary Mergers Observed by LIGO and Virgo during the First and Second Observing Runs, *Phys. Rev. X* **9**, 031040 (2019), [arXiv:1811.12907 \[astro-ph.HE\]](https://arxiv.org/abs/1811.12907).

[2] R. Abbott *et al.* (LIGO Scientific, Virgo), GWTC-2: Compact Binary Coalescences Observed by LIGO and Virgo During the First Half of the Third Observing Run, *Phys. Rev. X* **11**, 021053 (2021), [arXiv:2010.14527 \[gr-qc\]](https://arxiv.org/abs/2010.14527).

[3] R. Abbott *et al.* (LIGO Scientific, VIRGO), GWTC-2.1: Deep Extended Catalog of Compact Binary Coalescences Observed by LIGO and Virgo During the First Half of the Third Observing Run, (2021), [arXiv:2108.01045 \[gr-qc\]](https://arxiv.org/abs/2108.01045).

[4] R. Abbott *et al.* (LIGO Scientific, VIRGO, KAGRA), GWTC-3: Compact Binary Coalescences Observed by LIGO and Virgo During the Second Part of the Third Observing Run, (2021), [arXiv:2111.03606 \[gr-qc\]](https://arxiv.org/abs/2111.03606).

[5] M. Punturo *et al.*, The Einstein Telescope: A third-generation gravitational wave observatory, *Class. Quant. Grav.* **27**, 194002 (2010).

[6] S. Hild *et al.*, Sensitivity Studies for Third-Generation Gravitational Wave Observatories, *Class. Quant. Grav.* **28**, 094013 (2011), [arXiv:1012.0908 \[gr-qc\]](https://arxiv.org/abs/1012.0908).

[7] G. Janssen *et al.*, Gravitational wave astronomy with the SKA, *PoS AASKA14*, 037 (2015), [arXiv:1501.00127 \[astro-ph.IM\]](https://arxiv.org/abs/1501.00127).

[8] P. W. Graham, J. M. Hogan, M. A. Kasevich, and S. Rajendran, Resonant mode for gravitational wave detectors based on atom interferometry, *Phys. Rev. D* **94**, 104022 (2016), [arXiv:1606.01860 \[physics.atom-ph\]](https://arxiv.org/abs/1606.01860).

[9] P. Amaro-Seoane *et al.* (LISA), Laser Interferometer Space Antenna, (2017), [arXiv:1702.00786 \[astro-ph.IM\]](https://arxiv.org/abs/1702.00786).

[10] P. W. Graham, J. M. Hogan, M. A. Kasevich, S. Rajendran, and R. W. Romani (MAGIS), Mid-band gravitational wave detection with precision atomic sensors,

(2017), [arXiv:1711.02225 \[astro-ph.IM\]](https://arxiv.org/abs/1711.02225).

[11] L. Badurina *et al.*, AION: An Atom Interferometer Observatory and Network, *JCAP* **05**, 011, [arXiv:1911.11755 \[astro-ph.CO\]](https://arxiv.org/abs/1911.11755).

[12] Y. A. El-Neaj *et al.* (AEDGE), AEDGE: Atomic Experiment for Dark Matter and Gravity Exploration in Space, *EPJ Quant. Technol.* **7**, 6 (2020), [arXiv:1908.00802 \[gr-qc\]](https://arxiv.org/abs/1908.00802).

[13] A. Bertoldi *et al.*, AEDGE: Atomic experiment for dark matter and gravity exploration in space, *Exper. Astron.* **51**, 1417 (2021).

[14] I. Alonso *et al.*, Cold Atoms in Space: Community Workshop Summary and Proposed Road-Map (2022) [arXiv:2201.07789 \[astro-ph.IM\]](https://arxiv.org/abs/2201.07789).

[15] L. Badurina, O. Buchmueller, J. Ellis, M. Lewicki, C. McCabe, and V. Vaskonen, Prospective sensitivities of atom interferometers to gravitational waves and ultralight dark matter, *Phil. Trans. A. Math. Phys. Eng. Sci.* **380**, 20210060 (2021), [arXiv:2108.02468 \[gr-qc\]](https://arxiv.org/abs/2108.02468).

[16] M. Lewicki and V. Vaskonen, Impact of LIGO-Virgo binaries on gravitational wave background searches, (2021), [arXiv:2111.05847 \[astro-ph.CO\]](https://arxiv.org/abs/2111.05847).

[17] Z. Arzoumanian *et al.* (NANOGrav), The NANOGrav 12.5 yr Data Set: Search for an Isotropic Stochastic Gravitational-wave Background, *Astrophys. J. Lett.* **905**, L34 (2020), [arXiv:2009.04496 \[astro-ph.HE\]](https://arxiv.org/abs/2009.04496).

[18] B. Goncharov *et al.*, On the Evidence for a Common-spectrum Process in the Search for the Nanohertz Gravitational-wave Background with the Parkes Pulsar Timing Array, *Astrophys. J. Lett.* **917**, L19 (2021), [arXiv:2107.12112 \[astro-ph.HE\]](https://arxiv.org/abs/2107.12112).

[19] S. Chen *et al.*, Common-red-signal analysis with 24-yr high-precision timing of the European Pulsar Timing Array: inferences in the stochastic gravitational-wave background search, *Mon. Not. Roy. Astron. Soc.* **508**, 4970 (2021), [arXiv:2110.13184 \[astro-ph.HE\]](https://arxiv.org/abs/2110.13184).

[20] J. Antoniadis *et al.*, The International Pulsar Timing Array second data release: Search for an isotropic gravitational wave background, *Mon. Not. Roy. Astron. Soc.* **510**, 4873 (2022), [arXiv:2201.03980 \[astro-ph.HE\]](https://arxiv.org/abs/2201.03980).

[21] J. Ellis and M. Lewicki, Cosmic String Interpretation of NANOGrav Pulsar Timing Data, *Phys. Rev. Lett.* **126**, 041304 (2021), [arXiv:2009.06555 \[astro-ph.CO\]](https://arxiv.org/abs/2009.06555).

[22] S. Blasi, V. Brdar, and K. Schmitz, Has NANOGrav found first evidence for cosmic strings?, *Phys. Rev. Lett.* **126**, 041305 (2021), [arXiv:2009.06607 \[astro-ph.CO\]](https://arxiv.org/abs/2009.06607).

[23] V. Vaskonen and H. Veermäe, Did NANOGrav see a signal from primordial black hole formation?, *Phys. Rev. Lett.* **126**, 051303 (2021), [arXiv:2009.07832 \[astro-ph.CO\]](https://arxiv.org/abs/2009.07832).

[24] V. De Luca, G. Franciolini, and A. Riotto, NANOGrav Data Hints at Primordial Black Holes as Dark Matter, *Phys. Rev. Lett.* **126**, 041303 (2021), [arXiv:2009.08268 \[astro-ph.CO\]](https://arxiv.org/abs/2009.08268).

[25] Y. Nakai, M. Suzuki, F. Takahashi, and M. Yamada, Gravitational Waves and Dark Radiation from Dark Phase Transition: Connecting NANOGrav Pulsar Timing Data and Hubble Tension, *Phys. Lett. B* **816**, 136238 (2021), [arXiv:2009.09754 \[astro-ph.CO\]](https://arxiv.org/abs/2009.09754).

[26] W. Ratzinger and P. Schwaller, Whispers from the dark side: Confronting light new physics with NANOGrav data, *SciPost Phys.* **10**, 047 (2021), [arXiv:2009.11875 \[astro-ph.CO\]](https://arxiv.org/abs/2009.11875).

[27] K. Kohri and T. Terada, Solar-Mass Primordial Black Holes Explain NANOGrav Hint of Gravitational Waves, *Phys. Lett. B* **813**, 136040 (2021), [arXiv:2009.11853 \[astro-ph.CO\]](https://arxiv.org/abs/2009.11853).

[28] S. Vagnozzi, Implications of the NANOGrav results for inflation, *Mon. Not. Roy. Astron. Soc.* **502**, L11 (2021), [arXiv:2009.13432 \[astro-ph.CO\]](https://arxiv.org/abs/2009.13432).

[29] A. Neronov, A. Roper Pol, C. Caprini, and D. Semikoz, NANOGrav signal from magnetohydrodynamic turbulence at the QCD phase transition in the early Universe, *Phys. Rev. D* **103**, 041302 (2021), [arXiv:2009.14174 \[astro-ph.CO\]](https://arxiv.org/abs/2009.14174).

[30] J. J. Blanco-Pillado, K. D. Olum, and J. M. Wachter, Comparison of cosmic string and superstring models to NANOGrav 12.5-year results, *Phys. Rev. D* **103**, 103512 (2021), [arXiv:2102.08194 \[astro-ph.CO\]](https://arxiv.org/abs/2102.08194).

[31] D. Wang, Squeezing Cosmological Phase Transitions with International Pulsar Timing Array, (2022), [arXiv:2201.09295 \[astro-ph.CO\]](https://arxiv.org/abs/2201.09295).

[32] A. Roper Pol, C. Caprini, A. Neronov, and D. Semikoz, Gravitational wave signal from primordial magnetic fields in the Pulsar Timing Array frequency band, *Phys. Rev. D* **105**, 123502 (2022), [arXiv:2201.05630 \[astro-ph.CO\]](https://arxiv.org/abs/2201.05630).

[33] R. Z. Ferreira, A. Notari, O. Pujolas, and F. Rompineve, Gravitational Waves from Domain Walls in Pulsar Timing Array Datasets, (2022), [arXiv:2204.04228 \[astro-ph.CO\]](https://arxiv.org/abs/2204.04228).

[34] C. Caprini *et al.*, Science with the space-based interferometer eLISA. II: Gravitational waves from cosmological phase transitions, *JCAP* **04**, 001, [arXiv:1512.06239 \[astro-ph.CO\]](https://arxiv.org/abs/1512.06239).

[35] C. Caprini *et al.*, Detecting gravitational waves from cosmological phase transitions with LISA: an update, *JCAP* **03**, 024, [arXiv:1910.13125 \[astro-ph.CO\]](https://arxiv.org/abs/1910.13125).

[36] P. Auclair *et al.*, Probing the gravitational wave background from cosmic strings with LISA, *JCAP* **04**, 034, [arXiv:1909.00819 \[astro-ph.CO\]](https://arxiv.org/abs/1909.00819).

[37] N. Bartolo *et al.*, Science with the space-based interferometer LISA. IV: Probing inflation with gravitational waves, *JCAP* **12**, 026, [arXiv:1610.06481 \[astro-ph.CO\]](https://arxiv.org/abs/1610.06481).

[38] S. R. Coleman, The Fate of the False Vacuum. 1. Semi-classical Theory, *Phys. Rev. D* **15**, 2929 (1977), [Erratum: *Phys. Rev. D* 16, 1248 (1977)].

[39] A. Kosowsky and M. S. Turner, Gravitational radiation from colliding vacuum bubbles: envelope approximation to many bubble collisions, *Phys. Rev. D* **47**, 4372 (1993), [arXiv:astro-ph/9211004](https://arxiv.org/abs/astro-ph/9211004).

[40] M. Kamionkowski, A. Kosowsky, and M. S. Turner, Gravitational radiation from first order phase transitions, *Phys. Rev. D* **49**, 2837 (1994), [arXiv:astro-ph/9310044](https://arxiv.org/abs/astro-ph/9310044).

[41] M. Hindmarsh and M. Hijazi, Gravitational waves from first order cosmological phase transitions in the Sound Shell Model, *JCAP* **12**, 062, [arXiv:1909.10040 \[astro-ph.CO\]](https://arxiv.org/abs/1909.10040).

[42] D. Cutting, M. Hindmarsh, and D. J. Weir, Vorticity, kinetic energy, and suppressed gravitational wave production in strong first order phase transitions, *Phys. Rev. Lett.* **125**, 021302 (2020), [arXiv:1906.00480 \[hep-ph\]](https://arxiv.org/abs/1906.00480).

[43] M. Lewicki and V. Vaskonen, Gravitational wave spectra from strongly supercooled phase transitions, *Eur. Phys. J. C* **80**, 1003 (2020), [arXiv:2007.04967 \[astro-ph.CO\]](https://arxiv.org/abs/2007.04967).

[44] M. Lewicki and V. Vaskonen, Gravitational waves from colliding vacuum bubbles in gauge theories, *Eur. Phys. J. C* **81**, 437 (2021), [Erratum: *Eur. Phys. J. C* 81, 1077 (2021)], [arXiv:2012.07826 \[astro-ph.CO\]](https://arxiv.org/abs/2012.07826).

[45] R. Jinno, T. Konstandin, and H. Rubira, A hybrid simulation of gravitational wave production in first-order phase transitions, *JCAP* **04**, 014, arXiv:2010.00971 [astro-ph.CO].

[46] R. Jinno and M. Takimoto, Probing a classically conformal B-L model with gravitational waves, *Phys. Rev. D* **95**, 015020 (2017), arXiv:1604.05035 [hep-ph].

[47] S. Iso, P. D. Serpico, and K. Shimada, QCD-Electroweak First-Order Phase Transition in a Supercooled Universe, *Phys. Rev. Lett.* **119**, 141301 (2017), arXiv:1704.04955 [hep-ph].

[48] L. Marzola, A. Racioppi, and V. Vaskonen, Phase transition and gravitational wave phenomenology of scalar conformal extensions of the Standard Model, *Eur. Phys. J. C* **77**, 484 (2017), arXiv:1704.01034 [hep-ph].

[49] T. Prokopec, J. Rezacek, and B. Świeżewska, Gravitational waves from conformal symmetry breaking, *JCAP* **02**, 009, arXiv:1809.11129 [hep-ph].

[50] C. Marzo, L. Marzola, and V. Vaskonen, Phase transition and vacuum stability in the classically conformal B-L model, *Eur. Phys. J. C* **79**, 601 (2019), arXiv:1811.11169 [hep-ph].

[51] P. Baratella, A. Pomarol, and F. Rompineve, The Supercooled Universe, *JHEP* **03**, 100, arXiv:1812.06996 [hep-ph].

[52] B. Von Harling, A. Pomarol, O. Pujolàs, and F. Rompineve, Peccei-Quinn Phase Transition at LIGO, *JHEP* **04**, 195, arXiv:1912.07587 [hep-ph].

[53] M. Aoki and J. Kubo, Gravitational waves from chiral phase transition in a conformally extended standard model, *JCAP* **04**, 001, arXiv:1910.05025 [hep-ph].

[54] L. Delle Rose, G. Panico, M. Redi, and A. Tesi, Gravitational Waves from Supercool Axions, *JHEP* **04**, 025, arXiv:1912.06139 [hep-ph].

[55] X. Wang, F. P. Huang, and X. Zhang, Phase transition dynamics and gravitational wave spectra of strong first-order phase transition in supercooled universe, *JCAP* **05**, 045, arXiv:2003.08892 [hep-ph].

[56] J. Ellis, M. Lewicki, and V. Vaskonen, Updated predictions for gravitational waves produced in a strongly supercooled phase transition, *JCAP* **11**, 020, arXiv:2007.15586 [astro-ph.CO].

[57] M. Lewicki, O. Pujolàs, and V. Vaskonen, Escape from supercooling with or without bubbles: gravitational wave signatures, *Eur. Phys. J. C* **81**, 857 (2021), arXiv:2106.09706 [astro-ph.CO].

[58] C. Grojean and G. Servant, Gravitational Waves from Phase Transitions at the Electroweak Scale and Beyond, *Phys. Rev. D* **75**, 043507 (2007), arXiv:hep-ph/0607107.

[59] G. C. Dorsch, S. J. Huber, and J. M. No, Cosmological Signatures of a UV-Conformal Standard Model, *Phys. Rev. Lett.* **113**, 121801 (2014), arXiv:1403.5583 [hep-ph].

[60] P. Huang, A. J. Long, and L.-T. Wang, Probing the Electroweak Phase Transition with Higgs Factories and Gravitational Waves, *Phys. Rev. D* **94**, 075008 (2016), arXiv:1608.06619 [hep-ph].

[61] M. Artymowski, M. Lewicki, and J. D. Wells, Gravitational wave and collider implications of electroweak baryogenesis aided by non-standard cosmology, *JHEP* **03**, 066, arXiv:1609.07143 [hep-ph].

[62] V. Vaskonen, Electroweak baryogenesis and gravitational waves from a real scalar singlet, *Phys. Rev. D* **95**, 123515 (2017), arXiv:1611.02073 [hep-ph].

[63] G. C. Dorsch, S. J. Huber, T. Konstandin, and J. M. No, A Second Higgs Doublet in the Early Universe: Baryogenesis and Gravitational Waves, *JCAP* **05**, 052, arXiv:1611.05874 [hep-ph].

[64] J. Ellis, M. Lewicki, and J. M. No, On the Maximal Strength of a First-Order Electroweak Phase Transition and its Gravitational Wave Signal, *JCAP* **04**, 003, arXiv:1809.08242 [hep-ph].

[65] A. Beniwal, M. Lewicki, M. White, and A. G. Williams, Gravitational waves and electroweak baryogenesis in a global study of the extended scalar singlet model, *JHEP* **02**, 183, arXiv:1810.02380 [hep-ph].

[66] M. Fairbairn, E. Hardy, and A. Wickens, Hearing without seeing: gravitational waves from hot and cold hidden sectors, *JHEP* **07**, 044, arXiv:1901.11038 [hep-ph].

[67] J. Ellis, M. Lewicki, J. M. No, and V. Vaskonen, Gravitational wave energy budget in strongly supercooled phase transitions, *JCAP* **06**, 024, arXiv:1903.09642 [hep-ph].

[68] M. Lewicki, M. Merchand, and M. Zych, Electroweak bubble wall expansion: gravitational waves and baryogenesis in Standard Model-like thermal plasma, *JHEP* **02**, 017, arXiv:2111.02393 [astro-ph.CO].

[69] R.-G. Cai and S.-J. Wang, Effective picture of bubble expansion, *JCAP* **03**, 096, arXiv:2011.11451 [astro-ph.CO].

[70] L. Darmé, J. Jaeckel, and M. Lewicki, Towards the fate of the oscillating false vacuum, *Phys. Rev. D* **96**, 056001 (2017), arXiv:1704.06445 [hep-ph].

[71] M. Lewicki, V. Vaskonen, and H. Veermäe, Bubble dynamics in fluids with N-body simulations, (2022), arXiv:2205.05667 [astro-ph.CO].

[72] D. Bodeker and G. D. Moore, Can electroweak bubble walls run away?, *JCAP* **05**, 009, arXiv:0903.4099 [hep-ph].

[73] D. Bodeker and G. D. Moore, Electroweak Bubble Wall Speed Limit, *JCAP* **05**, 025, arXiv:1703.08215 [hep-ph].

[74] A. Azatov and M. Vanyla, Bubble wall velocity: heavy physics effects, *JCAP* **01**, 058, arXiv:2010.02590 [hep-ph].

[75] S. Höche, J. Kozaczuk, A. J. Long, J. Turner, and Y. Wang, Towards an all-orders calculation of the electroweak bubble wall velocity, *JCAP* **03**, 009, arXiv:2007.10343 [hep-ph].

[76] M. Barroso Mancha, T. Prokopec, and B. Świeżewska, Field-theoretic derivation of bubble-wall force, *JHEP* **01**, 070, arXiv:2005.10875 [hep-th].

[77] J. R. Espinosa, T. Konstandin, J. M. No, and G. Servant, Energy Budget of Cosmological First-order Phase Transitions, *JCAP* **06**, 028, arXiv:1004.4187 [hep-ph].

[78] R. Jinno, H. Seong, M. Takimoto, and C. M. Um, Gravitational waves from first-order phase transitions: Ultra-supercooled transitions and the fate of relativistic shocks, *JCAP* **10**, 033, arXiv:1905.00899 [astro-ph.CO].

[79] A. Kurganov and E. Tadmor, New high-resolution central schemes for nonlinear conservation laws and convection-diffusion equations, *Journal of Computational Physics* **160**, 241 (2000).

[80] T. Konstandin, Gravitational radiation from a bulk flow model, *JCAP* **03**, 047, arXiv:1712.06869 [astro-ph.CO].

[81] R. Allahverdi *et al.*, The First Three Seconds: a Review of Possible Expansion Histories of the Early Universe 10.21105/astro.2006.16182 (2020), arXiv:2006.16182 [astro-ph.CO].

[82] N. Aghanim *et al.* (Planck), Planck 2018 results. VI. Cosmological parameters, *Astron. Astrophys.* **641**, A6

(2020), [Erratum: *Astron. Astrophys.* **652**, C4 (2021)], [arXiv:1807.06209 \[astro-ph.CO\]](https://arxiv.org/abs/1807.06209).

[83] C. Caprini, R. Durrer, T. Konstandin, and G. Servant, General Properties of the Gravitational Wave Spectrum from Phase Transitions, *Phys. Rev. D* **79**, 083519 (2009), [arXiv:0901.1661 \[astro-ph.CO\]](https://arxiv.org/abs/0901.1661).

[84] R.-G. Cai, S. Pi, and M. Sasaki, Universal infrared scaling of gravitational wave background spectra, *Phys. Rev. D* **102**, 083528 (2020), [arXiv:1909.13728 \[astro-ph.CO\]](https://arxiv.org/abs/1909.13728).

[85] G. Barenboim and W.-I. Park, Gravitational waves from first order phase transitions as a probe of an early matter domination era and its inverse problem, *Phys. Lett. B* **759**, 430 (2016), [arXiv:1605.03781 \[astro-ph.CO\]](https://arxiv.org/abs/1605.03781).

[86] A. Hook, G. Marques-Tavares, and D. Racco, Causal gravitational waves as a probe of free streaming particles and the expansion of the Universe, *JHEP* **02**, 117, [arXiv:2010.03568 \[hep-ph\]](https://arxiv.org/abs/2010.03568).

[87] Y. Gouttenoire, G. Servant, and P. Simakachorn, Kinetic cosmology from scalar fields and gravitational-wave signatures, (2021), [arXiv:2111.01150 \[hep-ph\]](https://arxiv.org/abs/2111.01150).